








## Adsorption-controlled growth of $\text{MnTe}(\text{Bi}_2\text{Te}_3)_n$ by molecular beam epitaxy exhibiting stoichiometry-controlled magnetism

Jason Lapano <sup>1</sup>, Lauren Nuckols <sup>2</sup>, Alessandro R. Mazza <sup>1</sup>, Yun-Yi Pai <sup>1</sup>, Jie Zhang <sup>1</sup>, Ben Lawrie <sup>1</sup>, Rob G. Moore,<sup>1</sup> Gyula Eres,<sup>1</sup> Ho Nyung Lee,<sup>1</sup> Mao-Hua Du,<sup>1</sup> T. Zac Ward,<sup>1</sup> Joon Sue Lee,<sup>3</sup> William J. Weber <sup>2</sup>, Yanwen Zhang,<sup>1,2</sup> and Matthew Brahlek<sup>1,\*</sup>

<sup>1</sup>Materials Science and Technology Division, Oak Ridge National Laboratory, Oak Ridge, Tennessee 37831, USA

<sup>2</sup>Department of Materials Science and Engineering, University of Tennessee, Knoxville, Tennessee 37996, USA

<sup>3</sup>Department of Physics and Astronomy, University of Tennessee, Knoxville, Tennessee 37996, USA



(Received 15 September 2020; accepted 20 October 2020; published 11 November 2020)

We report the growth of the intrinsic magnetic topological system  $\text{MnTe}(\text{Bi}_2\text{Te}_3)_n$  by molecular beam epitaxy. By mapping the temperature and the Bi:Mn flux ratio, it is shown that there is a narrow growth window for the  $n = 1$  phase  $\text{MnBi}_2\text{Te}_4$  with  $2.0 < \text{Bi} : \text{Mn} < 2.6$  at 225 °C. Here the films are stoichiometric and excess Bi and Te is not incorporated. At higher flux ratios ( $\text{Bi}:\text{Mn} \geq 4.5$ ) it is found that the  $n = 2$   $\text{MnBi}_4\text{Te}_7$  phase is stabilized. Transport measurements indicate that the  $\text{MnBi}_2\text{Te}_4$  and  $\text{MnBi}_4\text{Te}_7$  undergo magnetic transitions around 25 and 10 K, respectively, consistent with antiferromagnetic phases found in the bulk. Further, for Mn-rich conditions ( $\text{Bi}:\text{Mn} < 2$ ), ferromagnetism emerges that exhibits a clear hysteretic state in the Hall effect, which likely indicates Mn-doped  $\text{MnBi}_2\text{Te}_4$ . Understanding how to grow ternary chalcogenide phases is the key to synthesizing new materials and to interface magnetism and topology, which together are routes to realize and control exotic quantum phenomena.

DOI: [10.1103/PhysRevMaterials.4.111201](https://doi.org/10.1103/PhysRevMaterials.4.111201)

Finding materials that exhibit multiple phenomena that are coupled gives deep insight into the physics of complex materials. Further, this can enable routes to design and engineer new technologies where modifying one state may induce switching in the other. Key examples are when a material is magnetic while concurrently (or incipiently) superconducting [1–5], ferroelectric [6–9], or more recently topological [10–14]. This latter example is of fundamental interest since magnetic ordering can be used to modify the topological class by changing the band structure [15–17]. Prominent examples are a Weyl semimetal phase that emerges from a 3D Dirac semimetal when ferromagnetism is introduced [18–21], as well as the quantized anomalous Hall (QAH) phase that emerges out of topological insulators when time-reversal symmetry is broken [16,22–24]. From a materials viewpoint this can be achieved either through doping a topological material into a magnetic phase, interfacing it with a magnet as an atomic-scale heterostructure, or by finding a material that intrinsically exhibits both phases. While magnetic doping has proven very effective at realizing the QAH in Cr/V-doped  $(\text{Bi}_{1-x}\text{Sb}_x)_2\text{Te}_3$  [22,24], promising examples of the latter have recently emerged with the discovery of several classes of magnetic topological materials including Fe-Sn [25],  $\text{Co}_3\text{Sn}_2\text{S}_2$  [18,21], and, of interest to the current work, the  $\text{MnTe}(\text{Bi}_2\text{Te}_3)_n$  series [23,26–33].

The  $\text{MnTe}(\text{Bi}_2\text{Te}_3)_n$  series is especially interesting due to the simultaneous topological nature along with the layered A-type antiferromagnetic (AFM) ground state, which,

together, enabled the recent observation of the QAH in exfoliated bulk crystals of  $\text{MnBi}_2\text{Te}_4$  [23,26]. As shown in Fig. 1,  $\text{MnTe}(\text{Bi}_2\text{Te}_3)_n$ , which is a single member of a broader class of ternary chalcogenides [32], spans the  $n = 0$  phase of MnTe to the  $n = \infty$  phase of  $\text{Bi}_2\text{Te}_3$ . Between these end members, the structure is composed of interleaving Te-Bi-Te-Bi-Te ( $\text{Bi}_2\text{Te}_3$ ) quintuple layers (QLs) and Te-Bi-Te-Mn-Te-Bi-Te ( $\text{MnBi}_2\text{Te}_4$ ) septuple layers (SLs). For example, the  $n = 1$  phase is  $\text{MnBi}_2\text{Te}_4$  composed only of SL and the  $n = 2$  phase is  $\text{MnBi}_4\text{Te}_7$  composed of alternating SL and QL. The ability to synthesize well-controlled  $\text{MnTe}(\text{Bi}_2\text{Te}_3)_n$  thin films will enable tuning the magnetic ground state, and thus the topological phase; it would then be possible to manipulate functional responses of these coupled behaviors by designing heterostructures with other magnets or by controlling the thickness to be predominately even/odd numbers of layers (for an A-type antiferromagnetic odd numbers of layers have a net moment).

However, in contrast to many materials, synthesis of thin films of  $\text{MnTe}(\text{Bi}_2\text{Te}_3)_n$  has been confined to the  $n = 1$  phase, which requires alternate depositions of MnTe and  $\text{Bi}_2\text{Te}_3$  that, in turn, relies on mixing to form the SL structure [34]. Molecular beam epitaxy (MBE) is well known as the gold standard for thin-film growth and has been an enabling technology in the study of quantum transport phenomena in topological systems [22,35–37]. The caveat, however, is that for binaries and ternaries the growth of the best-quality materials occurs when one or more elements are volatile and can be supplied in excess. Otherwise the film can accumulate errors in stoichiometry as defects, which can easily be in the range of 1–10%. For the case of the  $\text{MnTe}(\text{Bi}_2\text{Te}_3)_n$  series,

\*brahlek@ornl.gov

it is conceivable that it can be grown with an adsorption-controlled growth window since both Bi and Te are relatively volatile. However, it is not clear if this is possible since the thermodynamic barrier to intergrowths (due to the layered nature) and antisite defects among Mn and Bi are expected to be relatively low [38]. Here, we report the growth of  $\text{MnTe}(\text{Bi}_2\text{Te}_3)_n$  by molecular beam epitaxy (MBE). For the  $n = 1$  phase ( $\text{MnBi}_2\text{Te}_4$ ), it is shown that the growth is adsorption controlled based on the Mn flux, where Bi and Te are supplied in excess, although narrow in both temperature and flux ratios. At higher fluxes the  $\text{MnBi}_4\text{Te}_7$  is stabilized. The films properties are in good agreement with data from stoichiometric bulk crystals from the perspective of x-ray diffraction (XRD), Rutherford backscattering spectroscopy (RBS), and magnetotransport. Further, for Mn-rich films clear ferromagnetism emerges, which, together with the  $\text{MnBi}_2\text{Te}_4$  structure, indicates Mn-doped  $\text{MnBi}_2\text{Te}_4$ . This work opens many routes for tuning magnetic topological phases through dimensionality and interfacial phenomena such as the quantized anomalous Hall effect, as well as establishing a route to grow layered ternary chalcogenide materials.

$\text{MnTe}(\text{Bi}_2\text{Te}_3)_n$  films were grown in a home-built MBE system with base pressure of  $<5 \times 10^{-10}$  Torr. The substrates used were (0001)  $\text{Al}_2\text{O}_3$ , which were heated to  $600^\circ\text{C}$  in the MBE chamber and annealed for 10 min prior to growth to clean the surface. Further, high-purity Bi, Mn, and Te were calibrated with an *in situ* quartz-crystal microbalance (QCM) to achieve the desired flux ratio. QCM measurements were cross calibrated against film thicknesses measured using x-ray reflectivity, which yielded a flux ratio accuracy of a few percent. Mn flux was kept constant at  $1.40 \times 10^{13} \text{ cm}^{-2} \text{ s}^{-1}$ , and the Bi and Te fluxes were set relative to this. Following this, the substrates were cooled to  $135^\circ\text{C}$  where three SL were deposited to aid in nucleation. During this step the cells were calibrated to supply the stoichiometric flux of  $\text{Bi} : \text{Mn} : \text{Te} = 1 : 2 : 4$ , to ensure all films had similar starting growth surfaces. The films were subsequently ramped to the upper growth temperature  $185 < T < 250^\circ\text{C}$ , where the final depositions took place. The Bi and Te cells were adjusted to supply the appropriate Bi:Mn flux ratio for the sample and a Te overpressure of 2–3 times the stoichiometric value to prevent Te deficiencies in the film. Following the deposition, the films were annealed at the growth temperature for 60 min with the Te shutter open.

To understand the structural evolution of  $\text{MnTe}(\text{Bi}_2\text{Te}_3)_n$  films as a function of the Bi:Mn flux ratio as well as the deposition temperature, XRD was performed on two series of samples using  $\text{Cu-K}\alpha$  x rays. Figure 2 shows the results for XRD  $2\theta$ - $\theta$  scans where the growth temperature was varied from 185 to  $250^\circ\text{C}$  for the flux fixed at  $\text{Bi} : \text{Mn} = 2$ , and the Bi:Mn flux ratio was varied from 1.0–5.0 with the temperature fixed at  $225^\circ\text{C}$ . The data in Fig. 2(a) show the temperature dependence with the flux in the range to form  $\text{MnBi}_2\text{Te}_4$  (thickness of  $7 \pm 1$  nm). For films grown at the lowest temperature,  $185^\circ\text{C}$ , the peaks that are resolved are consistent with the  $(003n)$  series of  $\text{Bi}_2\text{Te}_3$ , where  $n$  is an integer. These peaks are marked as solid blue circles. This result implies that at this low temperature Mn is incorporated on the Bi site and there is insufficient kinetics to form  $\text{MnBi}_2\text{Te}_4$ . Further, increasing the growth temperature to  $200^\circ\text{C}$  yielded new peaks which

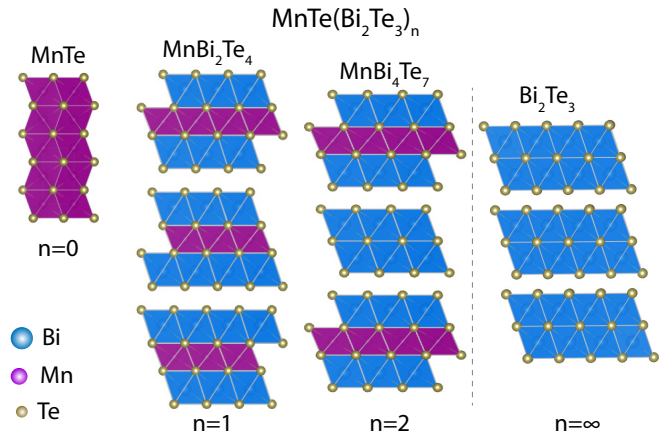


FIG. 1. Schematic crystal structures of the  $\text{MnTe}(\text{Bi}_2\text{Te}_3)_n$  system for various  $n$ .

are well separated from  $\text{Bi}_2\text{Te}_3$  peaks, specifically, around  $2\theta = 14^\circ, 35^\circ$ , and  $40^\circ$ . Upon further increasing the temperature to  $225^\circ\text{C}$ , these peaks became better resolved, and the intensity increased. This series of peaks matches very well to the  $(003n)$  series of the  $\text{MnBi}_2\text{Te}_4$  phase. Upon increasing the temperature to  $250^\circ\text{C}$ , additional peaks emerge around  $2\theta = 25^\circ$  and  $55^\circ$ . These are consistent with the formation of  $\text{MnTe}$  due to the desorption of volatile Bi-Te from the growing surface. Together this implies that all the Mn is adsorbed and the volatility of Bi and Te are controlling the phase formation.

To understand how the Bi-Te volatility controls the growth, Fig. 2(b) shows the detailed dependence of the  $2\theta$ - $\theta$  scans across a range of Bi:Mn fluxes with the temperature fixed at  $225^\circ\text{C}$  (the thickness of the samples are as follows with increasing Bi:Mn flux ratio: 15, 21, 23, 24, 29, 34, 41, 43,  $48 \pm 1$  nm). Postgrowth *in situ* reflection high-energy electron diffraction and *ex situ* atomic force microscopy images, given in Fig. S1 and S2 in Ref. [39], show the samples have flat 2D surfaces and are highly crystalline. Consider first  $2.0 < \text{Bi} : \text{Mn} < 2.6$ , which are shown in blue in Fig. 2(b). These curves exhibit the  $(003n)$  peaks of  $\text{MnBi}_2\text{Te}_4$  and the overall character is independent of the incident flux ratio. As discussed more below in the context of RBS measurements and transport, this suggests a growth window for  $\text{MnBi}_2\text{Te}_4$ . With increasing flux ratio beyond  $\text{Bi} : \text{Mn} = 2.6$ , the peaks appear to split as the next member of the series begins to form. This is highlighted in Fig. 2(b) by the vertical dashed arrows. The new pattern exactly matches  $\text{MnBi}_4\text{Te}_7$ , indicated as open green triangles. The larger number of peaks is due to the larger unit-cell height, which is increased by the addition of a QL unit in between the SLs, as shown in Fig. 1. For the two highest flux values shown (4.5 and 5.0) the peaks are nominally independent of flux ratio, which imply that a growth window may exist for this member. However, given the layered structure, precise homogeneous ordering is unlikely and will require more in-depth study at these higher fluxes. Finally, at fluxes below  $\text{Bi} : \text{Mn} = 2.0$ , shown in red, the  $\text{MnBi}_2\text{Te}_4$  phase clearly persists even down to the  $\text{Bi} : \text{Mn} = 1.0$ . This result is very surprising because, with excess Mn, the formation of  $\text{Mn}_{\text{Bi}}$  antisite defects (Mn on the Bi sites),  $\text{MnTe}$ , or a

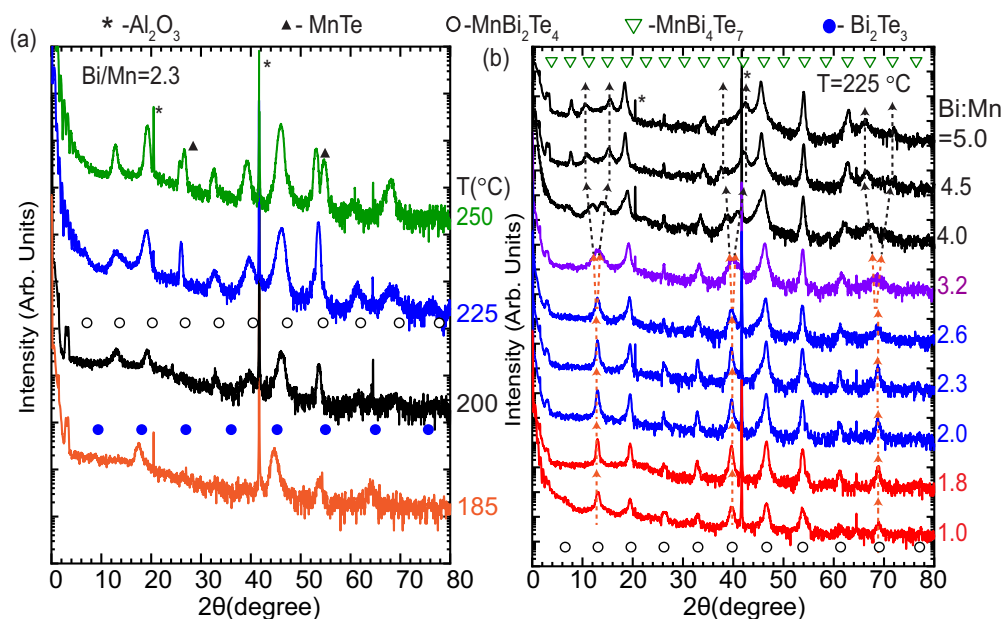


FIG. 2. X-ray diffraction  $2\theta$ - $\theta$  scans for (a) Bi:Mn flux ratio fixed at 2.3 at various growth temperatures and (b) temperature fixed at 225 °C for various Bi:Mn fluxes, with the exact flux ratio indicated on the right-hand axis. As indicated the peaks are marked as asterisks: Al<sub>2</sub>O<sub>3</sub>, solid triangles: MnTe, open circles: MnBi<sub>2</sub>Te<sub>4</sub>, open triangles: MnBi<sub>4</sub>Te<sub>7</sub>, and solid circles: Bi<sub>2</sub>Te<sub>3</sub>. Dashed vertical arrows highlight the emergence of MnBi<sub>4</sub>Te<sub>7</sub> in (b).

combination would be expected [38]. However, for the latter there is no sign of MnTe peaks in this measurement.

Although XRD scans indicate that there are windows in the Bi:Mn flux ratio where the different members form, this is not a direct measure of the film stoichiometry. More specifically, nonstoichiometry can be accommodated by the formation of defects while maintaining the crystalline phase. To show that the stoichiometry is indeed controlled, RBS measurements were performed, which directly probe the film stoichiometry to an error less than a few percent. The RBS results are shown in Fig. 3. RBS was performed at the ion-beam materials laboratory [40] with 2-MeV He beam at incident, exit and scattering angles of 45°, 70°, and 155°, respectively. The He ion energy and large incident/exit angles were used to improve the depth resolution and reduce the uncertainty in determining the elemental concentration of the thin films. Sample spectra are shown in Figs. 3(a) and 3(b), where the data are solid square symbols and the model fit is the solid red line. At low channel number the broad plateaus are oxygen (onset at channel ≈600) and Al (channel ≈1000) from the substrate, where the plateaulike peak shape indicates a continuous loss of energy as the He ions penetrate deep into the crystal. With increasing channel number, the additional peaks are Mn (channel ≈1400), Te (channel ≈1600), and Bi (channel ≈1700).

To extract the areal density of each individual species the RBS spectra were fit using the SIMNRA program [41]. Good fits, as shown in Figs. 3(a) and 3(b), were obtained for all the samples evaluated by RBS. The assumption of a thin film with a fixed stoichiometry used in SIMNRA fitting indicates a uniform film deposition and sharp interface. The results of the fitting are plotted versus the Bi:Mn flux onto the film surface in Fig. 3(c). This figure shows the atomic percentage,  $P(\%)$ , of Bi and Mn (the solid data points). Also shown are dashed lines

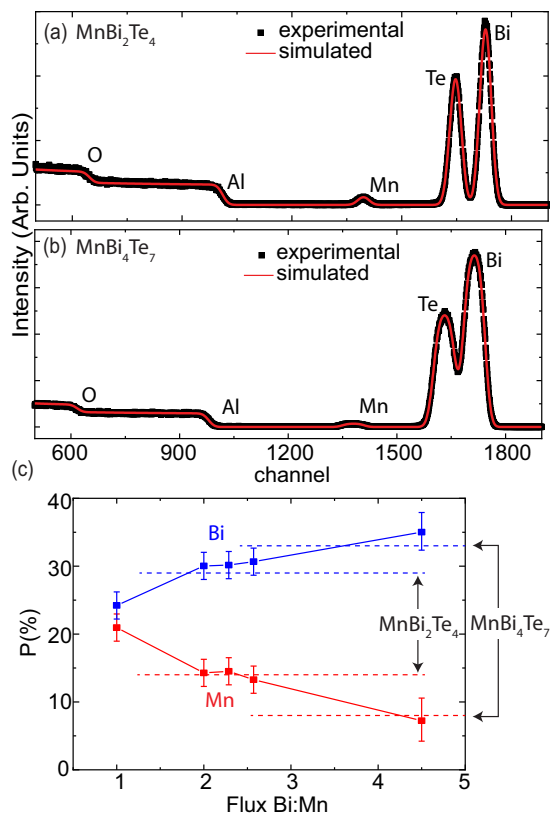


FIG. 3. (a), (b) RBS for two samples with flux ratio Bi : Mn = 2 (a) and 4.5 (b). (c) Results of fitting the spectra versus the flux incident on the sample where  $P(\%)$  is the atomic percentage of Mn (red) and Bi (blue). The horizontal dashed lines indicate the atomic percentages expected for MnBi<sub>2</sub>Te<sub>4</sub> and MnBi<sub>4</sub>Te<sub>7</sub>.

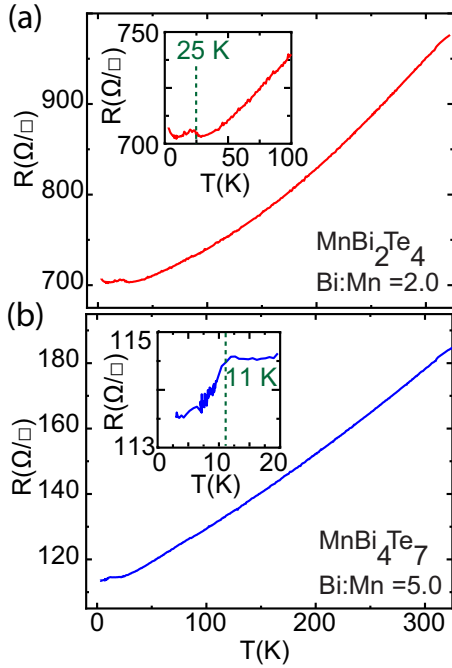


FIG. 4. (a), (b) Resistance versus temperature plots for  $\text{MnBi}_2\text{Te}_4$  with Bi : Mn = 2.0 (a) and  $\text{MnBi}_4\text{Te}_7$  with Bi : Mn = 5.0 (b). The insets highlight the low-temperature transport where the kinks indicate the magnetic transition, highlighted by the vertical dashed lines.

that indicate the ideal atomic percentage for  $\text{MnBi}_2\text{Te}_4$  and  $\text{MnBi}_4\text{Te}_7$ . For  $2.0 < \text{Bi} : \text{Mn} < 2.6$ , the atomic percentage of the film is found to be very close to the ideal value expected for  $\text{MnBi}_2\text{Te}_4$ . This supports the analysis from XRD, which showed peaks consistent with this phase. The fact that the film stoichiometry is nominally the same with increasing flux of Bi implies that the excess Bi and Te are desorbed off the growing surface rather than incorporated. Further, the flux ratio of Bi : Mn = 4.5 similarly shows that the film stoichiometry agrees well with  $\text{MnBi}_4\text{Te}_7$ . Finally, on the lower end of Bi:Mn, the stoichiometry is found to be roughly 1:1. This is very surprising since the predominate phase found in XRD is that of  $\text{MnBi}_2\text{Te}_4$ , without features of MnTe. This implies that there may be a large stability window for the formation of  $\text{MnBi}_2\text{Te}_4$  despite high levels of nonstoichiometry.

Figures 4(a) and 4(b) show detailed temperature-dependent transport data for the films grown at 225 °C from 300 K down to 2 K for Bi : Mn = 2.0 and 5.0, respectively. Here, these data are shown in sheet resistance  $R(\Omega/\square)$  rather than resistivity [ $\rho = R(\Omega/\square) \times \text{thickness}$ ] due to the convolution of the bulk states and surface states. Both samples show metallic behavior, where the resistance decreases with decreasing temperature. The resistance for  $\text{MnBi}_2\text{Te}_4$  films is found to be significantly larger than  $\text{MnBi}_4\text{Te}_7$ . This can be attributed to the structure of  $\text{MnBi}_4\text{Te}_7$  which is composed of interleaved SL and QL where the additional layer of  $\text{Bi}_2\text{Te}_3$  likely provides higher conductivity pathways. Further, this coincides with transport data from bulk crystals where the low-temperature resistivity of the  $\text{MnBi}_2\text{Te}_4$  is around 1 m $\Omega$  cm and  $\text{MnBi}_4\text{Te}_7$  is around 0.4 m $\Omega$  cm [42,43], which agrees

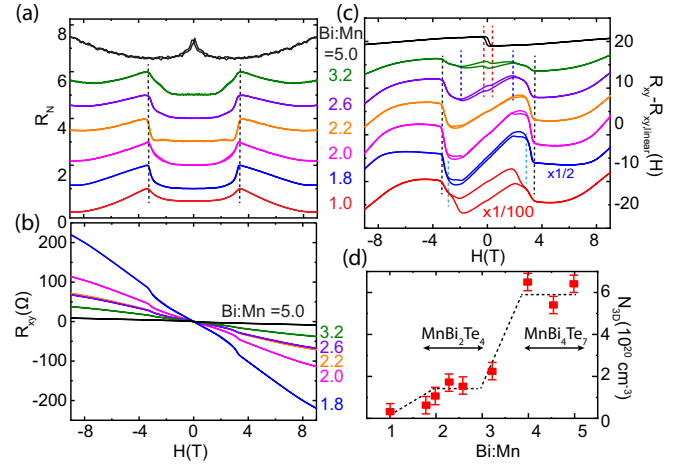


FIG. 5. (a), (b) Normalized magnetoresistance  $R_N = (R_S - R_{S,\text{Min}})/(R_{S,\text{Max}} - R_{S,\text{Min}})$  (a) and Hall resistance  $R_{xy}$  (b) versus magnetic field for various Bi:Mn flux ratios taken at 3 K. (c) Hall resistance in (b) with the linear portion subtracted. Vertical dashed lines indicate magnetic transitions; see main text for details and discussion. (a)–(c) Bi : Mn = 1.0–2.6 exhibit the  $\text{MnBi}_2\text{Te}_4$  phase, while Bi : Mn > 3.2 exhibits  $\text{MnBi}_4\text{Te}_7$ . (d) Carrier concentration extracted from the Hall effect at 150 K versus Bi:Mn ratio.

well with 1.63 m $\Omega$  cm for the  $\text{MnBi}_2\text{Te}_4$  film and 0.55 m $\Omega$  cm for the  $\text{MnBi}_4\text{Te}_7$  film. Finally, the magnetic transitions can be clearly identified in Figs. 4(a) and 4(b) as kinks. These are highlighted in the insets where the kinks occur roughly at 25 K for  $\text{MnBi}_2\text{Te}_4$  and 11 K for  $\text{MnBi}_4\text{Te}_7$ , which, again, agree well with the bulk.

Figures 5(a) and 5(b) show the magnetic field dependence of the transport at 3 K for various Bi:Mn flux ratios where the samples were measured in van der Pauw geometry. Here the magnetic field,  $H$ , is applied in the out-of-plane direction along the crystallographic  $c$  axis. Shown in Fig. 5(a) is the rescaled magnetoresistance  $R_N = (R - R_{\text{Min}})/(R_{\text{Max}} - R_{\text{Min}})$ , where  $R_{\text{Min}}$  and  $R_{\text{Max}}$  are the maximum and minimum resistance, respectively, which have been offset for clarity. Plotting in this way enables a direct comparison of the shape and field dependence across the full range in fluxes. For the flux ranges of Bi : Mn = 1.0 – 3.2 the curves are found to be nominally the same, independent of the flux ratio. These are found to be quite flat between the applied fields of  $-2$  to 2 T. At  $|H| > 3.0$  T,  $R_N$  turns upward with increasing field and peaks at a local maximum. Beyond this field  $R_N$  decreases until around 8 T where there is an upturn and  $R_N$  increases with increasing field. The local maximum in  $R_N$  coincides with the behavior in the Hall effect versus flux ratio which shows a kink that occurs in the same field range; see Fig. 5(b). In comparison to bulk data, this can be associated with the spin-flop phase transition where the spins on the Mn sites, initially oriented along the  $c$  axis, flip 90° and point in plane [43]. For the sample with Bi : Mn = 5.0,  $R_N$  is found to be dramatically different. At low field this sample shows a slight negative magnetoresistance with a small hysteresis around  $|H| < 0.2$  T. This is consistent with the observations in bulk crystals. Finally, in comparison to bulk samples for  $\text{MnBi}_2\text{Te}_4$ , while the magnetic ordering temperature and magnetic field scales for the spin-flop

transition are similar to bulk samples, the overall curve shape differs. In bulk crystals and exfoliated flakes, the magnetoresistance is nominally flat at low magnetic fields and undergoes a steep drop at the spin-flop transition and a weak peak at the spin-flip transition around 8 T [43–45]. However, the shape of the magnetoresistance is found to match closely to that of exfoliated flakes where the carrier concentration has been tuned with an external gate electrode, with virtually no peak at higher field that indicates the spin-flip transition [26]. It is noted that the overall resistance value observed here is significantly lower.

The Hall resistance  $R_{xy}$ , shown in Fig. 5(b), gives additional insight into the evolution of the magnetic phase and the defect density with Bi:Mn that compliments  $R_N$ . The overall trends can be more easily seen in Fig. 5(c) where a linear slope has been subtracted from the Hall resistance ( $R_{xy}-R_{xy,linear}$ ) and offset for clarity. First, for Bi : Mn = 2.0 and 2.2 the curves are nominally identical. This supports the XRD and RBS analysis for a narrow growth window for  $MnBi_2Te_4$ . This agrees well with data from bulk samples where the Hall resistance shows a steep drop at the spin-flop transition around  $H = 3.5$  T, and slight change in slope around 6–8 T. These transitions can clearly be seen in the plot of  $R_{xy}-R_{xy,linear}$ . The spin-flop transition is highlighted by vertical black dashed lines, nominally independent of flux, consistent with the dependence of  $R_N$ . Further, the upturn at around 6–8 T likely indicates the spin-flip transition. Both these transitions can clearly be resolved between Bi : Mn = 1.8–3.2. Moving to the highest flux ratio Bi : Mn = 5.0,  $R_{xy}-R_{xy,linear}$  shows only a slight hysteresis around  $|H| < 0.2$  T. This is consistent with the hysteresis found in  $R_N$  in Fig. 5(a) and agrees well with bulk data for  $MnBi_4Te_7$ . Interestingly, the samples with Bi : Mn = 2.6 and 3.2 show a low-field hysteresis that agrees with  $MnBi_4Te_7$ , highlighted by vertical red dashed lines. The low-field behavior of  $MnBi_4Te_7$  is superimposed on the spin-flop and spin-flip characteristic of  $MnBi_2Te_4$ , but also a slightly larger field hysteresis that closes at about 3 T, marked by vertical blue lines. This implies that within this intermediate regime there is a phase mixture, which is overall consistent with the XRD. Lastly, at the lowest flux ratio Bi : Mn = 1.0, a large hysteresis emerges, which is marked by vertical light-blue dashed lines. Since the XRD indicates that the phase is  $MnBi_2Te_4$ , this likely implies that this ferromagnetic phase is due to Mn doping of  $MnBi_2Te_4$ ; similarly, for Bi : Mn = 2.6 and 3.2, this may also explain the hysteresis that closes at around 2 T as Mn-doped  $MnBi_4Te_7$ .

Finally, shown in Fig. 5(d) is the carrier density,  $N_{3D}$ , extracted from the Hall effect at 150 K, well above the magnetic transition temperature, as shown in Fig. S3 of Ref. [39].  $N_{3D}$  can be separated into two different regimes. In the first regime, for Bi:Mn < 4, the structure extracted from XRD is  $MnBi_2Te_4$ , and  $N_{3d}$  shows a small increase with increasing Bi:Mn at low values, then a slight plateau just above Bi : Mn = 2. In the second regime, for values above Bi : Mn = 4, there is a significant increase in carrier concentration. This coincides with the formation of  $MnBi_4Te_7$  from XRD. In both regimes the carrier type is always found to be electronlike. The data are consistent with the expectation from bulk samples where the carrier concentration at room temperature is on the

order of  $1 \times 10^{20} \text{ cm}^{-3}$  for  $MnBi_2Te_4$  [43] and  $6 \times 10^{20} \text{ cm}^{-3}$  for  $MnBi_4Te_7$  [42]. At these high densities the Fermi level is well into the conduction band. In comparison to the  $n = \infty$  members such as  $Bi_2Te_3$ , carrier densities can be much lower than observed here. Further, in both of these materials, antisite-type  $Bi_{Mn}^+$  and  $Mn_{Bi}^-$  defects will form to compensate nonstoichiometries as vacancies and interstitials are too high in energy [38]. Excess Bi will lead to the formation of  $Bi_{Mn}^+$  donors which will raise  $N_{3d}$ ; while Mn excess creates  $Mn_{Bi}^-$  acceptors, which will lower  $N_{3D}$  and move the Fermi level closer to the conduction-band minimum. This is reflected in the data with the trend of increased carrier concentration as the Bi:Mn ratio is increased in the  $MnBi_2Te_4$ , and may also explain how the samples are able to remain in the  $MnBi_2Te_4$  structure at Bi:Mn < 2. This highlights the challenge in synthesizing these more complex structures of  $MnBi_2Te_4$  and  $MnBi_4Te_7$ , where charged antisite defects occur with large density and are highly dependent on film stoichiometry [38]. Finding suitable conditions that minimize such defects while maintaining phase purity represents the next challenge for this class of materials. MBE growth, however, offers several routes to tune the global Fermi level. This includes utilizing *in situ* virtual substrate methods that reduce interfacial defects [36] and alloying with  $MnSb_2Te_4$  to balance acceptor and donor antisite defects where the  $n$ -type to  $p$ -type crossover occurs around  $x = 0.63$  in  $Mn(Bi_{1-x}Sb_x)_2Te_4$  [46].

To conclude, we have shown the growth of  $MnTe(Bi_2Te_3)_n$  by MBE. This utilizes a two-step growth sequence where a low-temperature layer was deposited with stoichiometric flux ratio, which was followed by a higher-temperature deposition where excess Bi and Te evaporate. Using this method, the  $n = 1$  ( $MnBi_2Te_4$ ) and  $n = 2$  ( $MnBi_4Te_7$ ) can be stabilized. Additionally, we have shown the  $MnBi_2Te_4$  phase can be grown in excess Bi-Te flux. However, the growth window is relatively narrow in both temperature and flux. The resulting films are found to be single phase by XRD and stoichiometric by RBS. Moreover, transport properties are in good agreement with bulk crystals of  $MnBi_2Te_4$  and  $MnBi_4Te_7$  with magnetic transitions at around 25 and 11 K, respectively. Understanding how to synthesize this class of materials by MBE opens a huge space for engineering magnetism and topological states in a single material without the need for doping other elements. Moreover, this can enable functional tuning by integration as heterostructures with ferromagnetic and antiferromagnetic materials, both of which can exhibit a wide variety of transition temperatures, moments, orderings, and domain structures. These together can enable realization of exotic phases or raise the temperature where such phases can be observed, with a particular emphasis on the QAH phase. Towards this goal many challenges remain. Of key importance is controlling the Fermi level, which requires a deeper understanding of what defects form and under what conditions. Achieving such goals will open many routes to control this material family and guide stabilizing other exotic systems as high-quality thin films by MBE.

*Note added in Proof.* Recently, we become aware Refs. [47,48], which report  $MnBi_2Te_4$  grown with a codeposition approach.

The Department of Energy will provide public access to these results of federally sponsored research in accordance with the DOE Public Access Plan [49].

#### ACKNOWLEDGMENTS

This work has been partially supported by the U.S. Department of Energy, Office of Science, Basic Energy Sciences, Materials Sciences and Engineering Division (MBE growth, transport, and x-ray diffraction), and by the Laboratory Directed Research and Development Program of

Oak Ridge National Laboratory managed by UT-Battelle, LLC, under Contract No. DE-AC05-00OR22725 for the U.S. Department of Energy (part of MBE growth). Ion-beam analysis was performed at the Ion Beam Materials Laboratory located at the University of Tennessee, Knoxville. Y.Z. acknowledges support from Energy Dissipation to Defect Evolution (EDDE), an Energy Frontier Research Center funded by the U.S. Department of Energy, Office of Science, Basic Energy Sciences (RBS). We would like to thank Jiaqiang Yan for insightful discussions.

- 
- [1] W. E. Pickett, R. Weht, and A. B. Shick, *Phys. Rev. Lett.* **83**, 3713 (1999).
- [2] O. V. Dobrovolskiy, R. Sachser, T. Brächer, T. Böttcher, V. V. Kruglyak, R. V. Vovk, V. A. Shklovskij, M. Huth, B. Hillebrands, and A. V. Chumak, *Nat. Phys.* **15**, 477 (2019).
- [3] K. R. Jeon, C. Ciccirelli, A. J. Ferguson, H. Kurebayashi, L. F. Cohen, X. Montiel, M. Eschrig, J. W. A. Robinson, and M. G. Blamire, *Nat. Mater.* **17**, 499 (2018).
- [4] M. Iavarone, A. Scarfato, F. Bobba, M. Longobardi, G. Karapetrov, V. Novosad, V. Yefremenko, F. Giubileo, and A. M. Cucolo, *Phys. Rev. B* **84**, 024506 (2011).
- [5] A. V. Chumak, A. A. Serga, and B. Hillebrands, *J. Phys. D: Appl. Phys.* **50**, 244001 (2017).
- [6] J. H. Lee, L. Fang, E. Vlahos, X. Ke, Y. W. Jung, L. F. Kourkoutis, J. W. Kim, P. J. Ryan, T. Heeg, M. Roeckerath, V. Goian, M. Bernhagen, R. Uecker, P. C. Hammel, K. M. Rabe, S. Kamba, J. Schubert, J. W. Freeland, D. A. Muller, C. J. Fennie, P. Schiffer, V. Gopalan, E. Johnston-Halperin, and D. G. Schlom, *Nature (London)* **466**, 954 (2010).
- [7] W. Eerenstein, N. D. Mathur, and J. F. Scott, *Nature (London)* **442**, 759 (2006).
- [8] J. Hemberger, P. Lunkenheimer, R. Fichtl, S. Weber, V. Tsurkan, and A. Loidl, *Phys. B: Condens. Matter* **378-380**, 363 (2006).
- [9] T. Lottermoser, T. Lonkai, U. Amann, D. Hohlwein, J. Ihringer, and M. Fiebig, *Nature (London)* **430**, 541 (2004).
- [10] M. Mogi, M. Kawamura, R. Yoshimi, A. Tsukazaki, Y. Kozuka, N. Shirakawa, K. S. Takahashi, M. Kawasaki, and Y. Tokura, *Nat. Mater.* **16**, 516 (2017).
- [11] Y. Tokura, K. Yasuda, and A. Tsukazaki, *Nat. Rev. Phys.* **1**, 126 (2019).
- [12] Q. L. He, X. Kou, A. J. Grutter, G. Yin, L. Pan, X. Che, Y. Liu, T. Nie, B. Zhang, and S. M. Disseler *et al.*, *Nat. Mater.* **16**, 94 (2017).
- [13] Y. L. Chen, J.-H. Chu, J. G. Analytis, Z. K. Liu, K. Igarashi, H.-H. Kuo, X. L. Qi, S. K. Mo, R. G. Moore, D. H. Lu, M. Hashimoto, T. Sasagawa, S. C. Zhang, I. R. Fisher, Z. Hussain, and Z. X. Shen, *Science* **329**, 659 (2010).
- [14] X. Yao, B. Gao, M. G. Han, D. Jain, J. Moon, J. W. Kim, Y. Zhu, S. W. Cheong, and S. Oh, *Nano Lett.* **19**, 4567 (2019).
- [15] X.-L. Qi, T. L. Hughes, and S.-C. Zhang, *Phys. Rev. B* **78**, 195424 (2008).
- [16] R. Yu, W. Zhang, H.-J. J. Zhang, S.-C. C. Zhang, X. Dai, and Z. Fang, *Science* **329**, 61 (2010).
- [17] N. P. Armitage, E. J. Mele, and A. Vishwanath, *Rev. Mod. Phys.* **90**, 015001 (2018).
- [18] N. Morali, R. Batabyal, P. K. Nag, E. Liu, Q. Xu, Y. Sun, B. Yan, C. Felser, N. Avraham, and H. Beidenkopf, *Science* **365**, 1286 (2019).
- [19] S. M. Huang, S. Y. Xu, I. Belopolski, C. C. Lee, G. Chang, B. Wang, N. Alidoust, G. Bian, M. Neupane, C. Zhang, S. Jia, A. Bansil, H. Lin, and M. Z. Hasan, *Nat. Commun.* **6**, 7373 (2015).
- [20] B. Q. Lv, H. M. Weng, B. B. Fu, X. P. Wang, H. Miao, J. Ma, P. Richard, X. C. Huang, L. X. Zhao, G. F. Chen, Z. Fang, X. Dai, T. Qian, and H. Ding, *Phys. Rev. X* **5**, 031013 (2015).
- [21] Q. Xu, E. Liu, W. Shi, L. Muechler, J. Gayles, C. Felser, and Y. Sun, *Phys. Rev. B* **97**, 235416 (2018).
- [22] C. Z. Chang, J. Zhang, X. Feng, J. Shen, Z. Zhang, M. Guo, K. Li, Y. Ou, P. Wei, L. L. Wang, Z. Q. Ji, Y. Feng, S. Ji, X. X. Chen, J. Jia, X. X. Dai, Z. Fang, S. C. Zhang, K. He, Y. Wang, L. L. Lu, X. C. Ma, and Q. K. Xue, *Science* **340**, 167 (2013).
- [23] Y. Deng, Y. Yu, M. Z. Shi, Z. Guo, Z. Xu, J. Wang, X. H. Chen, and Y. Zhang, *Science* **367**, 895 (2020).
- [24] C. Z. Chang, W. Zhao, D. Y. Kim, H. Zhang, B. A. Assaf, D. Heiman, S. C. Zhang, C. Liu, M. H. W. Chan, and J. S. Moodera, *Nat. Mater.* **14**, 473 (2015).
- [25] J. A. Paulson, M. Kang, L. Ye, S. Fang, J.-S. You, A. Levitan, M. Han, J. I. Facio, C. Jozwiak, A. Bostwick, E. Rotenberg, M. K. Chan, R. D. McDonald, D. Graf, K. Kaznatcheev, E. Vescovo, D. C. Bell, E. Kaxiras, J. van den Brink, M. Richter, M. Prasad Ghimire, J. G. Checkelsky, and R. Comin, *Nat. Mater.* **19**, 163 (2020).
- [26] C. Liu, Y. Wang, H. Li, Y. Wu, Y. Li, J. Li, K. He, Y. Xu, J. Zhang, and Y. Wang, *Nat. Mater.* **19**, 522 (2020).
- [27] P. Swatek, Y. Wu, L.-L. Wang, K. Lee, B. Schruck, J. Yan, and A. Kaminski, *Phys. Rev. B* **101**, 161109 (2020).
- [28] Y.-J. Hao, P. Liu, Y. Feng, X.-M. Ma, E. F. Schwier, M. Arita, S. Kumar, C. Hu, R. Lu, M. Zeng, Y. Wang, Z. Hao, H.-Y. Sun, K. Zhang, J. Mei, N. Ni, L. Wu, K. Shimada, C. Chen, Q. Liu, and C. Liu, *Phys. Rev. X* **9**, 041038 (2019).
- [29] C. Hu, L. Ding, K. N. Gordon, B. Ghosh, H. Li, S.-W. Lian, A. G. Linn, H.-J. Tien, C.-Y. Huang, P. V. S. Reddy, B. Singh, A. Agarwal, A. Bansil, S.-Y. Xu, H. Lin, H. Cao, T.-R. Chang, D. Dessau, and N. Ni, *Sci. Adv.* **6**, eaba4275 (2020).
- [30] Z. S. Aliev, I. R. Amiraslanov, D. I. Nasonova, A. V. Shevelkov, N. A. Abdullayev, Z. A. Jahangirli, E. N. Orujlu, M. M. Otrokov, N. T. Mamedov, M. B. Babanly, and E. V. Chulkov, *J. Alloys Compd.* **789**, 443 (2019).
- [31] C. Hu, K. N. Gordon, P. Liu, J. Liu, X. Zhou, P. Hao, D. Narayan, E. Emmanouilidou, H. Sun, Y. Liu, H. Brawer, A. P. Ramirez, L. Ding, H. Cao, Q. Liu, D. Dessau, and N. Ni, *Nat. Commun.* **11**, 97 (2020).

- [32] J. Li, Y. Li, S. Du, Z. Wang, B. L. Gu, S. C. Zhang, K. He, W. Duan, and Y. Xu, *Sci. Adv.* **5**, eaaw5685 (2019).
- [33] N. H. Jo, L.-L. Wang, R.-J. Slager, J. Yan, Y. Wu, K. Lee, B. Schruk, A. Vishwanath, and A. Kaminski, *Phys. Rev. B* **102**, 045130 (2020).
- [34] Y. Gong, J. Guo, J. Li, K. Zhu, M. Liao, X. Liu, Q. Zhang, L. Gu, L. Tang, X. Feng, D. Zhang, W. Li, C. Song, L. Wang, P. Yu, X. Chen, Y. Wang, H. Yao, W. Duan, Y. Xu, S. C. Zhang, X. Ma, Q. K. Xue, and K. He, *Chin. Phys. Lett.* **36**, 076801 (2019).
- [35] A. A. Taskin, S. Sasaki, K. Segawa, and Y. Ando, *Adv. Mater.* **24**, 5581 (2012).
- [36] N. Koirala, M. Brahlek, M. Salehi, L. Wu, J. Dai, J. Waugh, T. Nummy, M.-G. G. Han, J. Moon, Y. Zhu, D. Dessau, W. Wu, N. P. Armitage, and S. Oh, *Nano Lett.* **15**, 8245 (2015).
- [37] M. J. Manfra, *Annu. Rev. Condens. Matter Phys.* **5**, 347 (2014).
- [38] M.-H. Du, J. Yan, V. R. Cooper, and M. Eisenbach, *Adv. Funct. Mater.* 2006515 (2020).
- [39] See Supplemental Material at <http://link.aps.org/supplemental/10.1103/PhysRevMaterials.4.111201> for additional data including reflection high-energy electron diffraction, atomic force microscopy, and Hall-effect measurements.
- [40] Y. Zhang, M. L. Crespillo, H. Xue, K. Jin, C. H. Chen, C. L. Fontana, J. T. Graham, and W. J. Weber, *Nucl. Instruments Methods Phys. Res., Sect. B* **338**, 19 (2014).
- [41] M. Mayer, *Am. Inst. Phys. Conf. Proc.* **475**, 541 (1999).
- [42] J.-Q. Yan, Y. H. Liu, D. S. Parker, Y. Wu, A. A. Aczel, M. Matsuda, M. A. McGuire, and B. C. Sales, *Phys. Rev. Mater.* **4**, 54202 (2020).
- [43] J.-Q. Yan, Q. Zhang, T. Heitmann, Z. Huang, K. Y. Chen, J.-G. Cheng, W. Wu, D. Vaknin, B. C. Sales, and R. J. McQueeney, *Phys. Rev. Mater.* **3**, 064202 (2019).
- [44] J. Cui, M. Shi, H. Wang, F. Yu, T. Wu, X. Luo, J. Ying, and X. Chen, *Phys. Rev. B* **99**, 155125 (2019).
- [45] B. Chen, F. Fei, D. Zhang, B. Zhang, W. Liu, S. Zhang, P. Wang, B. Wei, Y. Zhang, Z. Zuo, J. Guo, Q. Liu, Z. Wang, X. Wu, J. Zong, X. Xie, W. Chen, Z. Sun, S. Wang, Y. Zhang, M. Zhang, X. Wang, F. Song, H. Zhang, D. Shen, and B. Wang, *Nat. Commun.* **10**, 4469 (2019).
- [46] J. Q. Yan, S. Okamoto, M. A. McGuire, A. F. May, R. J. McQueeney, and B. C. Sales, *Phys. Rev. B* **100**, 104409 (2019).
- [47] K. Zhu, Y. Bai, X. Hong, Z. Geng, Y. Jiang, R. Liu, Y. Li, M. Shi, L. Wang, W. Li, Q. K. Xue, X. Feng, and K. He, *J. Phys. Condens. Matter* **32**, 475002 (2020).
- [48] P. Kagerer, C. I. Fornari, S. Buchberger, S. L. Morelhão, R. C. Vidal, A. Tcakaev, V. Zabolotnyy, E. Weschke, V. Hinkov, M. Kamp, B. Büchner, A. Isaeva, H. Bentmann, and F. Reinert, *J. Appl. Phys.* **128**, 135303 (2020).
- [49] <http://energy.gov/downloads/doe-public-access-plan>.